Supplementary Information: Streaming enhanced flow-mediated transport

Tejaswin Parthasarathy[1], Fan Kiat Chan[1], and Mattia Gazzola[1,2]†

[1]Mechanical Sciences and Engineering, University of Illinois at Urbana-Champaign, Urbana, IL 61801, USA

[2]National Center for Supercomputing Applications, University of Illinois at Urbana-Champaign, Urbana, IL 61801, USA

(Received xx; revised xx; accepted xx)

1. Viscous flow mediated interactions–Algorithm and numerics

We use the remeshed Vortex Method (rVM) algorithm described in Gazzola *et al.* (2011) to perform two and three dimensional viscous flow-structure interaction simulations. Here, we list our simulation methodology and parameters for reproducibility and completeness.

1.1. *Algorithm: Governing equation*

We consider incompressible viscous flows in an infinite domain (Σ) in which two density-matched moving rigid bodies are immersed. We denote with Ω_i & $\partial\Omega_i$ the support and boundaries of the solids. Then the flow is described by the incompressible Navier–Stokes equations in its velocity–vorticity form:

$$\frac{D\boldsymbol{\omega}}{Dt} = (\omega \cdot \nabla)\boldsymbol{u} + \nu\nabla^2\boldsymbol{\omega}, \qquad \boldsymbol{x} \in \Sigma \setminus \Omega_i \tag{1.1}$$

$$\nabla \cdot \mathbf{u} = 0 \tag{1.2}$$

where Σ is the computational domain, $\frac{D}{Dt}$ is the material derivative operator, ν is the kinematic viscosity, and $\boldsymbol{u}$ and $\boldsymbol{\omega}$ are the velocity and vorticity fields respectively. The velocity field is recovered from the vorticity field by solving the Poisson equation

$$\nabla^2\boldsymbol{u} = -\nabla \times \boldsymbol{\omega} \tag{1.3}$$

1.2. *Algorithm: Discretization*

We rely on remeshed Vortex Methods in solving these equations where vorticity fields $\boldsymbol{\omega}$ are discretized into vortex particles $\boldsymbol{\omega}_p$ characterized by their position $\boldsymbol{x}_p$, volume V_p and strength $\Gamma_p = \int_{V_p} \omega d\boldsymbol{x}$. The vortex advection by the velocity field $\boldsymbol{u}$ is achieved in a Lagrangian fashion described by

$$\frac{d\boldsymbol{x}}{dt} = \boldsymbol{u}_p \tag{1.4}$$

and vortex stretching and diffusion are then described by

$$\frac{d\Gamma_p}{dt} = \left[(\boldsymbol{\omega} \cdot \nabla)\boldsymbol{u} + \nu\nabla^2\boldsymbol{\omega}\right]_p \tag{1.5}$$

† Email address for correspondence: mgazzola@illinois.edu

A remeshing approach, in which a high order moment-conserving kernel is used for the back and forth interpolation between particles and grid, is taken to preserve good numerical accuracy and avoid Lagrangian distortion from diffusion and dispersion errors. This hybrid particle-mesh approach also adapts the stability properties of particle method, where the time step size is limited by the Lagrangian CFL condition (LCFL) such that $||\nabla \boldsymbol{u}^{n-1}||\Delta t^n \leqslant LCFL$ for explicit time integration schemes.

1.3. *Algorithm: Fluid–Structure Interaction*

We represent the immersed body by a mollified characteristic function $\chi(\boldsymbol{x})$ on the regular mesh such that $\chi(\boldsymbol{x}) = 1$ for $\boldsymbol{x} \in \Omega_s$ and $\chi(\boldsymbol{x}) = 0$ for $\boldsymbol{x} \in \Omega_f$, where Ω_s and Ω_f are the solid and fluid domain respectively. We enforce the no-slip boundary condition through the Brinkman penalization technique such that the Navier–Stokes equation is supplemented with a penalization force term that forces fluid velocity within the solid body to the body velocity. The Navier-Stokes equation in its velocity–vorticity form now reads

$$\frac{D\boldsymbol{\omega}}{Dt} = (\boldsymbol{\omega} \cdot \nabla)\boldsymbol{u} + \nu\nabla^2\boldsymbol{\omega} + \lambda\nabla \times (\chi_s(\boldsymbol{u}_s - \boldsymbol{u})) \quad \boldsymbol{x} \in \Omega \tag{1.6}$$

where $\lambda \gg 1$ is the penalization parameter and $\lambda\nabla \times (\chi_s(\boldsymbol{u}_s - \boldsymbol{u}))$ is the penalization term.

The action of the fluid on the solid body is prescribed through a projection approach (Gazzola *et al.* 2011), in which the solid body's translational $\boldsymbol{u}_T$ and angular $\dot{\theta}$ velocities are computed through conservation of momentum in the system. The body and fluid are updated in an alternating fashion such that for any one time step, the fluid equations are evolved inside and outside of the body while the body is kept stationary. Once computed, linear and angular momenta transferred to the body are computed from the fluid velocity field extended inside the body and the body velocities are recovered from

$$\boldsymbol{u}_T = \frac{1}{M_s}\int_{\Sigma} \rho^n \chi_s^n \boldsymbol{u}^n d\boldsymbol{x} \tag{1.7}$$

$$\dot{\theta}^n = \frac{1}{J_s^n}\int_{\Sigma} \rho^n \chi_s^n \left(\mathbf{x} - \mathbf{x}_{cm}^n\right) \times \mathbf{u}^n d\boldsymbol{x} \tag{1.8}$$

where M_s is the total mass of the body and $\boldsymbol{J}_s$ is the moment of inertia tensor.

1.4. *Algorithm: General method*

We summarize in Algorithm 1 the general method used in our software to solve (1.6) using a Godunov splitting approach.

1.5. *Algorithm: 3D validation*

To further extend the validation of our numerical method for streaming problems beyond two dimensions, we quantitatively compare our results from three-dimensional simulations of an oscillating cylinder (of infinite length achieved through periodic boundary condition in the axial direction) with prior theory and experiments. These comparisons are conducted in the Finite-outer Boundary Layer regime (FBL) regime, wherein we relate the DC boundary layer thickness (δ_{dc}, defined as the offset of the stagnation streamline from the cylinder surface, marked with dashed lines in the insets of figure 1a) to the inverse Womersley number $\alpha^{-1} = \sqrt{\nu/\omega}/r_{\mathrm{m}}$. Indeed, we observe quantitative agreement between the three-dimensional simulations and experiment (Lutz *et al.* 2005), theory (Bertelsen *et al.* 1973) as well as our two-dimensional simulations (figure 1a).

We then validate our three-dimensional simulations with spheroids of different aspect

Algorithm 1 General Method

$$\chi_s^n = \chi(\boldsymbol{x}_{cm}^n, \theta^n, t^n) \tag{1.9}$$
$$\nabla^2 \psi^n = -\omega^n \tag{1.10}$$
$$\mathbf{u}^n = \nabla \times \psi^n \tag{1.11}$$
$$\mathbf{u}_T^n = \frac{1}{M_s} \int_\Sigma \rho^n \chi_s^n \mathbf{u}^n d\mathbf{x} \tag{1.12}$$
$$\dot{\theta}^n = \frac{1}{J_s^n} \int_\Sigma \rho^n \chi_s^n \left(\mathbf{x} - \mathbf{x}_{cm}^n\right) \times \mathbf{u}^n d\mathbf{x} \tag{1.13}$$
$$\mathbf{u}_R^n = \dot{\theta}^n \times (\mathbf{x} - \mathbf{x}_{cm}^n) \tag{1.14}$$
$$\mathbf{u}_\lambda^n = \frac{\mathbf{u}^n + \lambda \Delta t \chi_s^n \left(\mathbf{u}_T^n + \mathbf{u}_R^n\right)}{1 + \lambda \Delta t \chi_s^n} \tag{1.15}$$
$$\omega_\lambda^n = \nabla \times \mathbf{u}_\lambda^n \tag{1.16}$$
$$\frac{\partial \omega_\lambda^n}{\partial t} = \nu \nabla^2 \omega_\lambda^n \tag{1.17}$$
$$\frac{\partial \omega_\lambda^n}{\partial t} + \nabla \cdot \left(\mathbf{u}_\lambda^n \, \omega_\lambda^n\right) = 0 \tag{1.18}$$
$$\omega^{n+1} = \omega_\lambda^{n+1} \tag{1.19}$$
$$\mathbf{x}_{cm}^{n+1} = \mathbf{x}_{cm}^n + \mathbf{u}_T^n \Delta t^n \tag{1.20}$$
$$\theta^{n+1} = \theta^n + \dot{\theta}^n \Delta t^n \tag{1.21}$$

ratios (AR = a/b where a and b are the spheroid half-dimension along and normal to the axis of oscillation, respectively). Here, we again compare quantitatively the normalized distance δ_{dc} between the body surface and the stagnation point (averaged between the left and right) as indicated by the red bullets in the insets of figure 1b. We then relate these offsets of stagnation points to the Womersley number squared $\alpha^2 = \omega L^2/\nu$, where the spheroid length scale is defined here as $L = (\mathrm{AR})(b^2 a)^{1/3}$. We report the results of our measurements from simulations in figure 1b and observe good agreement with experimental data and its corresponding fitting (Kotas *et al.* 2007).

1.6. *Algorithm: Implementation and resources*

The algorithm in two-dimensions is implemented in C++-11 and relies on the Intel$^{(R)}$ Threading Building Block library for multi-threading within a shared-memory computer, on the FFTW3 (Fast Fourier Transform in the West) library (parallelized using OpenMP$^{(R)}$) for computing discrete Fourier transforms (to solve the Poisson equation), and on the VTK (Visualization ToolKit) library for visualization/post-processing. Each simulation is typically run for 8–48 hours on a single node (XE Cray, AMD6276 Interlagos processor with peak speed 2.45 GHz, with 16 physical (and 32 hyper-threaded) cores having 4GB memory each) on the BlueWaters supercomputing cluster.

The algorithm in three-dimensions is implemented in Fortran90 and relies on MPI for distributed memory parallelism. The software is built as a client of the Parallel Particle Mesh library (PPM) (Sbalzarini *et al.* 2006), which offers a convenient abstraction layer over MPI for particle–mesh operations, mapping on processors, processor communication and load-balancing. The software also relies on the FFTW3 library for Poisson solves as well as HDF library for visualization/post-processing. Three dimensional simulation

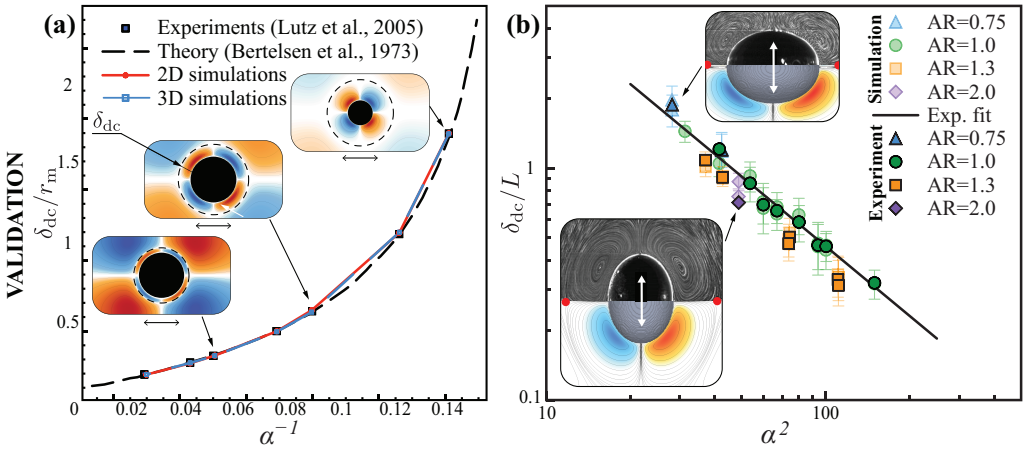

FIGURE 1. Validation for the 3D viscous flow solver: Comparison with experiments and theory in which we relate the DC boundary layer thickness δ_{dc} (suitably normalized) and Womersley number α (a) against an oscillating cylinder (Lutz *et al.* 2005; Bertelsen *et al.* 1973) and (b) against oscillating spheroids of varying aspect ratios AR (Kotas *et al.* 2007).

performed in this paper typically run for 8–48 hours on 8 nodes on the BlueWaters supercomputing cluster.

1.7. *2D simulation details*

We simulate the master (diameter $D_m = 0.111$m) and the slave (diameter $D_s = 0.028$m) in a domain of physical size $[0,1]^2$ m^2, with constant grid size of 2048×2048 in the x and y directions. The master is initialized at $\boldsymbol{x}_m^0 = [0.104, 0.5]$ m and moves laterally with a constant velocity of $U_l = |D_m|$ ms^{-1}. The slave is initialized at a surface-to-surface distance of $0.1D_m$ m behind the master at $\boldsymbol{x}_s^0 = [0.023, 0.5]$ m. The choice of the diameters and initial locations for the cylinders is made to maximize the resolution across both master and slave for a given simulation and for the non-dimensionless end time $T = 2U_l t/D_m = 15$. The number of grid points across the diameter of the master and slave are kept constant at 226 and 56 respectively. The viscosity ν is set based on the linear Reynolds number $Re = U_l D_m/\nu$. We oscillate the master with a fixed amplitude $A = \frac{1}{2}\epsilon D_m$, while the angular frequency ω is determined through the oscillatory Reynolds number $R_o = \zeta Re = \epsilon\omega D_m/(2\nu)$. We note that that both cylinders are density matched, with $\rho = 1$ kgm^{-3}.

1.8. *3D simulation details*

We simulate both the master and slave as spheres of diameter $D_m = 0.025$m and $D_s = 0.00625$m in an unbounded domain with uniform spacing of $1/2048$ m in each dimension. The master is initialized at $\boldsymbol{x}_m^0 = [0.2, 0, 0]$ m and moves laterally with a constant velocity of $U_l = |2D_m|$ms^{-1}. The slave is initialized at a surface-to-surface distance of $0.1D_m$ m behind the master at $\boldsymbol{x}_s^0 = [0.182, 0, 0]$ m. The simulation is set to stop at non-dimensional end time $T = 2U_l t/D_m = 24$. The viscosity ν is set based on the linear motion Reynolds number $Re = U_l D_m/\nu$. We oscillate the master with a fixed amplitude $A = \frac{1}{2}\epsilon D_m$, where $\epsilon = 0.05$, with an angular frequency ω determined by the oscillatory Reynolds number $R_o = \zeta Re = \epsilon\omega D_m/(2\nu)$. We note that both master and slave are density matched, with $\rho = 1$ kgm^{-3}.

2. Two dimensional inviscid flow mediated interactions–Algorithm and numerics

We discuss the numerical strategy used for the potential flow simulations and validate it against two benchmark problems. We once again consider two dimensional incompressible flow in an unbounded domain (Σ), in which n moving rigid bodies are immersed. We denote with Ω_i & $\partial\Omega_i$, $i = 1, \cdots n$ the support and boundaries of the solids, which are assumed to be of the same density of the fluid ($\rho_i = \rho = 1$ kgm^{-3}). We further define $\partial\Omega := \bigcup_{i=1}^{n} \partial\Omega_i$. The algorithm is the same as Munnier & Pinçon (2010), with minor modifications to simulate our master–slave systems.

2.1. *Algorithm: Governing equations*

The governing equations for the fluid in the inviscid limit are the Euler equations coupled with the incompressibility constraint:

$$\frac{\partial \boldsymbol{u}}{\partial t} + (\boldsymbol{u} \cdot \boldsymbol{\nabla})\, \boldsymbol{u} = -\frac{1}{\rho}\nabla P \qquad \boldsymbol{x} \in \Sigma \setminus \Omega \tag{2.1}$$

$$\boldsymbol{\nabla} \cdot \boldsymbol{u} = 0 \qquad \boldsymbol{x} \in \Sigma \setminus \Omega \tag{2.2}$$

The rigid solid body dynamics can be obtained by solving the Newton's equations of motion concurrently:

$$m_i \ddot{\boldsymbol{x}}_i = \boldsymbol{F}_i^H \tag{2.3}$$

$$\frac{d(I_i \dot{\theta}_i)}{dt} = \boldsymbol{M}_i^H \tag{2.4}$$

The causal force and moments in (2.3) and (2.4) on the body result from the boundary conditions that couple the fluid–solid dynamics:

$$\boldsymbol{u} \cdot \boldsymbol{n}(\boldsymbol{x}) = \boldsymbol{u}_i \cdot \boldsymbol{n}(\boldsymbol{x}) \qquad \boldsymbol{x} \in \partial\Omega_i \tag{2.5}$$

where $\boldsymbol{n}$ is the unit normal pointing towards the fluid and $\boldsymbol{u_i}$ is the velocity of the rigid body i, respectively. This encodes the no-through flow boundary condition.

To solve the above problem numerically we couch the solids and fluid systems into a larger one and solve for the total dynamics. This bypasses the need to calculate pressure and surface forces on the body as they are internal forces in the bigger system. As shown in Lamb (1932), one can adopt a Lagrangian perspective and solve for the total dynamics using the principle of minimal work (resulting in Euler–Lagrange equations). The dynamics (an initial value problem) then evolve in time according to the coupling between the solids and fluid (a boundary value problem). For the purpose of exposition we focus first on this coupling and then on evolving the system in time.

The idea is to simplify the non-linear problem (2.1) in the absence of initial ($t = 0$) vorticity using Helmholtz's theorem—which guarantees that vorticity remains absent in the flow at all times $t > 0$. We can then represent the conservative velocity vector as the gradient of a scalar potential function $\phi(\boldsymbol{x})$, i.e. $\nabla\phi(\boldsymbol{x}) = \boldsymbol{u}(\boldsymbol{x})$. As the velocity vector is always solenoidal (from (2.2))—the problem of solving (2.1) and (2.2) is cast to equivalently solving the following Laplace equation.

$$\nabla^2 \phi(\boldsymbol{x}) = 0 \qquad \boldsymbol{x} \in \Sigma \setminus \Omega \tag{2.6}$$

with the boundary conditions

$$\nabla\phi(\boldsymbol{x}) \cdot \boldsymbol{n}(\boldsymbol{x}) = (\boldsymbol{u}_i + \dot{\theta}_i \times (\boldsymbol{x} - \boldsymbol{x}_i) \cdot \boldsymbol{n}(\boldsymbol{x}), \qquad \boldsymbol{x} \in \partial\Omega_i \tag{2.7}$$

$$\nabla\phi(\boldsymbol{x}) = 0, \quad \boldsymbol{x} \to \infty \tag{2.8}$$

where $\dot{\theta}_i, \boldsymbol{x}_i$ represent the angular velocity and the center of the rigid body i. We thus solve an exterior Neumann Boundary Value Problem (NBVP), with (2.8) necessitating the flow decay at large distances. Following Lamb (1932), we decompose the potential field $\phi(\boldsymbol{x})$ into elementary Kirchhoff potentials $\mathcal{X}_i(\boldsymbol{x})$, $\boldsymbol{\varphi_i}(\boldsymbol{x})$ such that

$$\phi(\boldsymbol{x}) = \sum_{i=1}^{n} (\dot{\theta}_i \cdot \mathcal{X}_i(\boldsymbol{x}) + \boldsymbol{u}_i \cdot \boldsymbol{\varphi_i}(\boldsymbol{x})) \tag{2.9}$$

While this linear decomposition increases the algorithmic complexity of the problem, it enables us to separate the individual contribution from every rigid body velocity component in the flow. This is useful in calculating the added mass contributions resulting from the adjacent fluid being accelerated by the motion of the immersed solid bodies. The inertia (or) the mass matrix for the system $\boldsymbol{M}$ thus consists of the solid body inertia and added mass (fluid) contributions. $\boldsymbol{M}$ is a block matrix with the blocks $\boldsymbol{M}_{ij}$ given by

$$\boldsymbol{M}_{ij} = \begin{bmatrix} \int_{\Sigma\setminus\Omega} \nabla\mathcal{X}_i \cdot \nabla\mathcal{X}_j & \int_{\Sigma\setminus\Omega} \nabla\mathcal{X}_i \cdot \nabla\varphi_j^1 & \int_{\Sigma\setminus\Omega} \nabla\mathcal{X}_i \cdot \nabla\varphi_j^2 \\ \int_{\Sigma\setminus\Omega} \nabla\varphi_i^1 \cdot \nabla\mathcal{X}_j & \int_{\Sigma\setminus\Omega} \nabla\varphi_i^1 \cdot \nabla\varphi_j^1 & \int_{\Sigma\setminus\Omega} \nabla\varphi_i^1 \cdot \nabla\varphi_j^2 \\ \int_{\Sigma\setminus\Omega} \nabla\varphi_i^2 \cdot \nabla\mathcal{X}_j & \int_{\Sigma\setminus\Omega} \nabla\varphi_i^2 \cdot \nabla\varphi_j^1 & \int_{\Sigma\setminus\Omega} \nabla\varphi_i^2 \cdot \nabla\varphi_j^2 \end{bmatrix} + \begin{bmatrix} I_j\delta_{ij} & 0 & 0 \\ 0 & m_j\delta_{ij} & 0 \\ 0 & 0 & m_j\delta_{ij} \end{bmatrix} \tag{2.10}$$

where $i, j \in \{1, \cdots, n\}$ represent the i^{th} and j^{th}body contributions, $\boldsymbol{\varphi}$ has $[\varphi^1, \varphi^2]$ as its components, δ_{ij} represents the Kronecker-delta function and the $\boldsymbol{x}$ dependence on the integrands is implicit. This block captures the total finite inertia resulting from the presence and motion of both the moving bodies i, j and the fluid surrounding them, thus rendering it important for the collective dynamics of the system.

This dynamics evolve according to the Euler–Lagrange formula, where we consider the total system energy functional as the Lagrangian function to minimize. The kinematic energy of the i^{th} solid body is $K_i = \frac{1}{2}m_i|\boldsymbol{u}_i|^2 + \frac{1}{2}I_i\dot{\theta}_i^2$. The total kinematic energy of the fluid is $K_f = \frac{1}{2}\rho\int_{\Sigma\setminus\Omega_i} |\nabla\phi|^2(\boldsymbol{x})d\boldsymbol{x}$. In this work we do not consider conservative barotropic forces and so the potential energy contribution is identically zero. The total system energy functional is thus $L(\boldsymbol{q}, \dot{\boldsymbol{q}}) = K_f + K_1 + K_2 = \frac{1}{2}\dot{\boldsymbol{q}}^T\boldsymbol{M}(\boldsymbol{q})\dot{\boldsymbol{q}}$—a function of the state $\boldsymbol{q}$ and its derivative $\dot{\boldsymbol{q}}$. Here $\boldsymbol{q}$ represents the degrees of freedom for the system i.e. the angular and Cartesian positions of all the bodies (i.e. $\boldsymbol{q} = [\boldsymbol{q}_1, \cdots, \boldsymbol{q}_n]$ with $\boldsymbol{q}_i = [\theta_i \quad x_i^1 \quad x_i^2], i \in \{1, \cdots, n\}$). Using this Lagrangian function L we derive the Euler Lagrange equation for the state $\boldsymbol{q}$

$$\frac{d}{dt}\frac{\partial L}{\partial \dot{\boldsymbol{q}}} - \frac{\partial L}{\partial \boldsymbol{q}} = 0 \tag{2.11}$$

which equivalently results in

$$\boldsymbol{M}\ddot{\boldsymbol{q}} + \langle \Gamma(\boldsymbol{q}), \dot{\boldsymbol{q}}, \dot{\boldsymbol{q}} \rangle = 0 \tag{2.12}$$

where $\Gamma(\boldsymbol{q})$ is a rank-3 tensor identified as the Christoffel symbol (Munnier & Pinçon 2010) and $\langle \Gamma(\boldsymbol{q}), \dot{\boldsymbol{q}}, \dot{\boldsymbol{q}} \rangle$ is shorthand for $\Gamma(\boldsymbol{q})_{ij}^k \dot{q}_j \dot{q}_k$. If M_{ij} denotes the (i, j) entry of $\boldsymbol{M}$ $(i, j \in \{1, \cdots, 3n\})$ and q_i denotes the entries of $\boldsymbol{q}$ $(i \in \{1, \cdots, 3n\})$, then we define the Christoffel symbol Γ_{ij}^k by

$$\Gamma_{ij}^k = \frac{1}{2}\left(\frac{\partial M_{ki}}{\partial q_j} + \frac{\partial M_{kj}}{\partial q_i} - \frac{\partial M_{ij}}{\partial q_k}\right) \tag{2.13}$$

These 'shape derivative' $\frac{\partial M}{\partial q}$ terms are calculated efficiently according to the formulation in Munnier & Pinçon (2010). With all the above manipulations that follow from Lamb

(1932); Nair & Kanso (2007); Munnier & Pinçon (2010), we have reduced the governing nonlinear PDEs (2.1) and (2.2) to a system of nonlinear ODEs (2.12) which can be integrated efficiently in time.

2.2. *Algorithm: Representation*

To solve the NBVP (2.6), (2.7) and (2.8) at every timestep, we use Boundary Element Methods (BEMs) based on integral formulations of the Laplace equation. BEMs for the Laplace equation only need to be discretized on the surface—making them fast and efficient—thus eluding the problem of remeshing at every time step. The conversion of (2.6) to (2.8) to a formulation convenient for BEM is carried out by using Green's theorem, that reduces all volume integrals in (2.10) to surface integrals:

$$\int_{\Sigma\setminus\Omega} \nabla\mathcal{T}_i \cdot \nabla\mathcal{T}_j d\boldsymbol{x} = \tfrac{1}{2}\int_{\partial\Omega_j} \mathcal{T}_i \partial_{\boldsymbol{n}}\mathcal{T}_j d\sigma_j + \tfrac{1}{2}\int_{\partial\Omega_i} \mathcal{T}_j \partial_{\boldsymbol{n}}\mathcal{T}_i d\sigma_i \tag{2.14}$$

where $\mathcal{T}$ is a proxy for any of $\mathcal{X}, \varphi^1, \varphi^2$. Having transformed the volume Laplace problem to the equivalent boundary integral form, we realize that we only need the elementary Kirchhoff potentials on the boundaries $\partial\Omega_i$ (that is the Dirichlet data), given its normal derivatives (the Neumann data, from (2.7)). We then represent, discretize and solve for $\mathcal{T}$ on the boundaries only. The representation of elementary potentials of body i is done using finite terms (with cardinality m) of a Fourier series on $\partial\Omega_i$—the choice of the basis reflects the compact support and periodicity (with period 2π) of $\partial\Omega_i$.

We obtain the Dirichlet data (and its tangential derivatives) on the boundary using the Neumann-to-Dirichlet operator (Atkinson 1967) for the 2D Laplace kernel $G(\boldsymbol{x},\boldsymbol{y}) = \frac{1}{2\pi}\int_{\partial\Omega_i} \log|\boldsymbol{x}-\boldsymbol{y}| d\sigma_{\boldsymbol{y}}$. This reads for $i \in \{1,\cdots n\}$ and $\boldsymbol{x} \in \partial\Omega$

$$\mathcal{T}_i(\boldsymbol{x}) - \frac{1}{\pi}\int_{\partial\Omega} \frac{(\boldsymbol{y}-\boldsymbol{x})}{|\boldsymbol{y}-\boldsymbol{x}|^2}\cdot\boldsymbol{n}(\boldsymbol{y})\mathcal{T}_i(\boldsymbol{y}) d\sigma_{\boldsymbol{y}} = -\frac{1}{\pi}\int_{\partial\Omega_i} \log|\boldsymbol{y}-\boldsymbol{x}| N_i(\boldsymbol{y}) d\sigma_{\boldsymbol{y}} \tag{2.15}$$

where we have prescribed $N_i(\boldsymbol{y})$—the Neumann data from (2.7). The tangential derivatives of $\mathcal{T}_i$ are necessary to calculate the shape derivatives. This is trivially done as once $\mathcal{T}_i \in C^\infty$ is known, we can take its derivative in the tangential direction efficiently by using the spectral equivalent of the standard differentiation operator.

2.3. *Algorithm: Discretization and Implementation*

To solve the integral equation (2.15), we use Nyström discretization coupled with the (spectrally accurate) trapezoidal quadrature rule. To numerically evaluate the integrals, we split the integrand into singular and non-singular contributions and use the scheme suggested in Atkinson (1967) to evaluate the former—the latter is trivial to integrate numerically. The interested reader is referred to Atkinson (1967) for the theoretical and Munnier & Pinçon (2010) for the implementation details. We discretize the boundary $\partial\omega_i$ by $\upsilon_i = 2m_i+1$ points, where m_i is the finite number of Fourier modes represented on the boundary. We represent (2.15) in the discrete form by the equation $\boldsymbol{A}\boldsymbol{t} = \boldsymbol{r}$, where $\boldsymbol{t},\boldsymbol{r}$ are the discrete equivalents of $\mathcal{T}$ and the right hand side being solved for. We factorize $\boldsymbol{A}$ by standard LU-decomposition for the reasons listed in Munnier & Pinçon (2010). Having evaluated the elementary potential on $\partial\Omega_i$, we proceed to evaluate the mass matrix (2.10) and the Christoffel symbols Γ (2.13) at these boundaries. The acceleration in (2.12) is then evaluated and the whole system can be marched forward in time.

We now deal with the time-marching scheme used in solving (2.12), which we rewrite

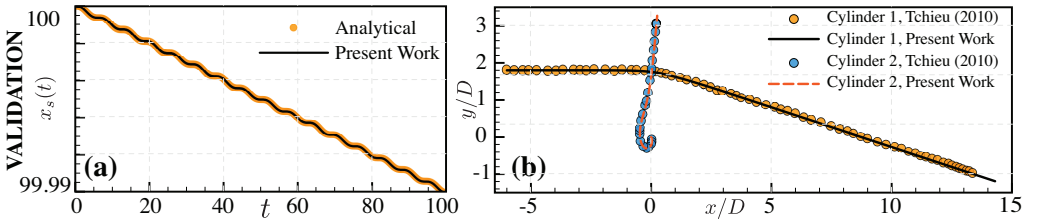

FIGURE 2. Validation for the potential flow solver : (a) against a purely oscillating master–slave configuration and (b) against a near-collision event of two free cylinders

as

$$\frac{d}{dt}\begin{bmatrix}\dot{\boldsymbol{q}}\\ \boldsymbol{q}\end{bmatrix} = \begin{bmatrix}-\boldsymbol{M}^{-1}\langle \Gamma(\boldsymbol{q}), \dot{\boldsymbol{q}}, \dot{\boldsymbol{q}}\rangle\\ \dot{\boldsymbol{q}}\end{bmatrix} \tag{2.16}$$

As the boundaries of the solids $\partial\Omega$ are assumed to be infinitely differentiable C^∞, parametrized with respect to a boundary tangent variable $t \in [0, 2\pi]$, we can infer that the RHS is then also C^∞. The above problem is then well posed and infinitely differentiable in time—making it a candidate for higher-order time stepping schemes. We use the `LSODA` function from `ODEPACK` (wrapped around and exposed as the `scipy.integrate.odeint` function in `Python`) that uses upto 13^{th} order accurate non-stiff (Adams) or stiff (BDF) method adaptively based on the data. We fix the absolute and relative tolerances of our ODE solver to 1.49×10^{-8}, unless stated otherwise. The algorithm is implemented in `Python` and relies on the vectorized routines of `numpy` and `scipy` for fast numerical linear algebraic and FFT calculations.

2.4. *Algorithm: Validation*

Here we consider two validation cases for our algorithm. The first benchmark case is the slave (radius b) motion due to pure sinusoidal oscillations of the master (radius a) in one direction, wherein we have a closed form governing ODE at large master–slave distances (Nair & Kanso 2007) for an inertialess master–slave pair. The slave transport is then purely due to the added-mass terms arising from the presence of the intermediate fluid. The nonlinear analytical ODE governing the slave position x_s for the case with $a = b = \sqrt{2}^{-1}$m, $\rho = \pi^{-1}$ kg m^{-3} and for pure sinusoidal oscillations of the master $x_\mathrm{m} = \sin(t)$ is

$$\ddot{x}_\mathrm{s} = -\frac{\sin t}{(x_\mathrm{s} - \sin t)^2} + \frac{2\cos^2 t}{(x_\mathrm{s} - \sin t)^3} \tag{2.17}$$

We now consider the same setup in our numerical solver using $\upsilon_i = 121$ points or $m_i = 60$ modes spatially on each cylinder (of density $\rho = 1 \times 10^{-8} \sim 0$ each) and step forward in time with a constant $\Delta t = 0.002$s. The result from the solution of the closed form nonlinear ODE (2.17) and our numerical solution, for an impulsively started master, is shown in figure 2(a). Our result matches the analytical result closely.

The second benchmark case is derived from Tchieu *et al.* (2010) and considers the near collision event of two 'free/passive' cylinders in the flow. In this case, two neutrally buoyant ($\rho_i = \rho = 1$ kg m^{-3}) cylinders, of diameter 1 m each are initially placed in the cartesian plane at $\boldsymbol{x}_1 = [-6.0 \quad 1.8]^T$ and $\boldsymbol{x}_2 = [0.0 \quad 0.0]^T$ respectively. The former is given an initial velocity of $\dot{\boldsymbol{x}}_1(0) = [1.0 \quad 0.0]^T$. It is noted that in the absence of the fluid both the cylinders will collide. The presence of the fluid acts as a 'cushion', and helps prevent collision between the cylinders. The cylinders then nearly kiss one another—and any singular effects associated with the near-contact event need to be well

resolved, making this a rigorous benchmark. We simulate this setup with our algorithm for $\upsilon_i = 121$ points each on the cylinders and with a constant $\Delta t = 0.002$s. The computed trajectory for both the cylinders is plotted in figure 2(b) against the one in Tchieu *et al.* (2010). The final velocity reported in Tchieu *et al.* (2010) for both the cylinders are $\dot{\boldsymbol{x}}_1(\infty) = [0.954 \quad -0.205]^T$ and $\dot{\boldsymbol{x}}_2(\infty) = [0.030 \quad 0.216]^T$ upto three significant digits. With our solver we get $\dot{\boldsymbol{x}}_1(\infty) = [0.954 \quad -0.205]^T$ and $\dot{\boldsymbol{x}}_2(\infty) = [0.029 \quad 0.216]^T$ as the final velocities. Our results are thus in close agreement.

2.5. *Simulation details*

Using the above algorithm, we seek to replicate the two dimensional neutrally-buoyant master–slave configurations described in the main text in a potential flow context. For such simulations, we use a master cylinder of diameter $D_\mathrm{m} = 1$m and a slave of diameter $D_\mathrm{s} = 0.25$m. The master is initially kept at $\boldsymbol{q}_\mathrm{m} = [0.0 \quad 0.0 \quad 0.0]^T$ and the slave is instantiated at $\boldsymbol{q}_\mathrm{s} = [0.0 \quad -0.725 \quad 0.0]^T$. The master is translated in the x direction and oscillated in the y direction. To avoid introducing impulse in the system (and thus eliminating bias) we ramp-up the motion of the master, as given by

$$x_\mathrm{m} = U_\mathrm{l}\left(t + \frac{1}{r}\ln\left(\frac{1+e^{r(c-t)}}{1+e^{rc}}\right)\right) \tag{2.18}$$

$$y_\mathrm{m} = \frac{\epsilon\omega D_\mathrm{m}\sin(\omega t)}{2\left(1+e^{r(c-t)}\right)} \tag{2.19}$$

where $r = \frac{28\epsilon\omega}{3\zeta}$ and $c = \frac{15\zeta}{14\omega\epsilon}$ are ramping parameters. We set, for all cases, $\epsilon = 0.05, \omega = 5$ and choose $U_\mathrm{l} = \frac{U_\mathrm{o}}{2\zeta} = \frac{\epsilon\omega D_\mathrm{m}}{4\zeta}$. We then only vary the velocity ratio ζ in our formulation in the simulations shown further below.

Unless stated otherise, we run all simulations with a constant time step $\Delta t = (200\pi)^{-1}T$, where $T = \frac{2\pi}{\omega}$ is the time period of oscillation. We use $\upsilon_i = 121$ or $m_i = 60$ fourier modes to capture the master–slave interactions.

3. Master–slave baseline transport

We first understand the baseline transport before introducing transverse oscillations. Here we discuss the initial setup of the system, validate our current simulations against the original results of Gazzola *et al.* (2012), and further investigate the sensitivity of baseline transport to *Re*.

3.1. *Initial master–slave separation distance*

Before validating and further analyzing the master–slave cylinder pair transport system, we first define the measure for separation distance between master and slave. While center-to-center (CC) distance may be a natural measure, we instead employ the surface-to-surface (SS) separation distance for the following reasons.

Firstly, fixing initial SS distance enables us to compare our results with those of previous works (Gazzola *et al.* 2012), which we drew upon to guide our analysis and exploration.

Secondly, both definitions are acceptable and at some level, arbitrary. For example, employing a constant initial SS distance ($0.1D_\mathrm{m}$ in this case) when exploring slave size effects would penalize large slaves (by increasing their CC distance, figure 3(b)). On the other hand, a constant initial CC distance would favor larger slaves, a portion of which would be in almost direct contact with the master. This is schematically shown

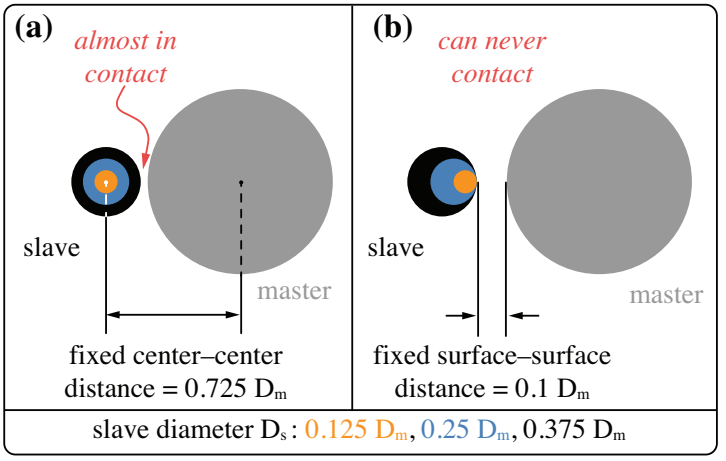

FIGURE 3. Master–slave schematic illustrating separation distance measured using *(a)* fixed center-to-center distance ($0.725D_\mathrm{m}$) and *(b)* fixed surface-to-surface distance ($0.1D_\mathrm{m}$) based on $D_\mathrm{s}/D_\mathrm{m} = 0.25$.

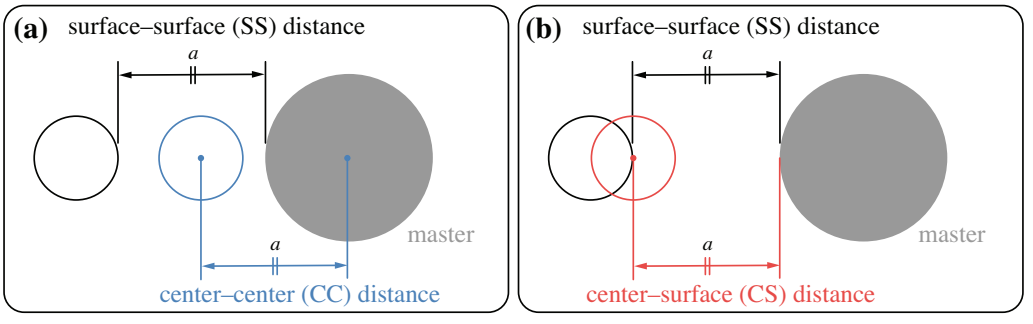

FIGURE 4. Master–slave schematic comparing *(a)* SS versus CC distance and *(b)* SS versus CS distance, illustrating that for a constant distance a, the CS measure falls in between SS and CC measures.

in figure 3(a). As an additional remark, we note that to partially overcome the above issue, we could also select the center–surface (CS) distance as an initialization measure (figure 4(b)). For a constant distance a, choosing this measure physically places the slave in between the SS and CC measures. Nonetheless, fundamentally this measure suffers from the same drawbacks.

Thirdly, fixing initial SS distance provides a lower bound for transport. That is, upon comparing configurations with the same initial SS and CC (and even CS) distance, the former (SS) provides a more conservative measure of assaying transport. In other words, if a slave is transported for SS $= a$, it is also transported for CS $= a$ and CC $= a$. Such a conservative estimate is useful in an engineering design context, in order to robustly dimension the system. To demonstrate that SS distance is a conservative choice, we carried out a cursory exploration of the ζ–Re phase space at $D_\mathrm{s}/D_\mathrm{m} = 0.125$ (all the other $D_\mathrm{s}/D_\mathrm{m}$ have similar behavior), by initializing slaves with same initial SS and CS distances, both $0.1D_\mathrm{m}$. CC distance is not considered here due to unphysical master–slave contact for CC $= 0.1D_\mathrm{m}$ (the slave is completely inside the master). We track once again the evolution of trapping/non-trapping thresholds (as done in section 4.1 in the main text) in these two cases, as shown in figure 5. As can be seen, the trapping thresholds for fixed CS distance $= 0.1D_\mathrm{m}$ (orange lines) move out, and are consequently wider than

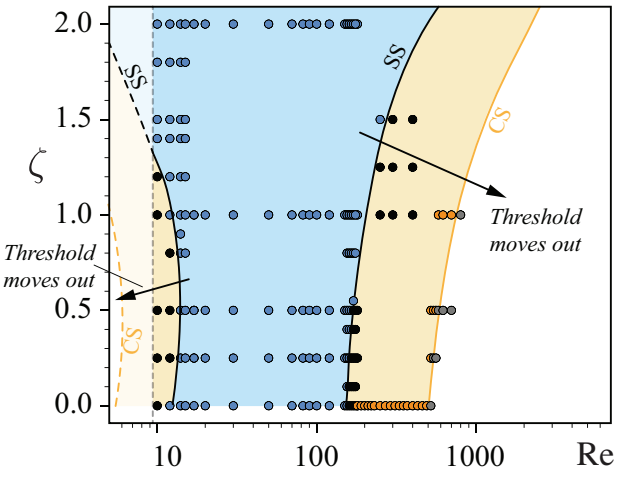

FIGURE 5. Comparisons of trapping (shaded region) and non-trapping (non-shaded region) thresholds on the ζ–Re phase space when two different initial separation distance measures are used, illustrating the larger extent of the trapping region when CS (orange region) is employed instead of SS (blue region) and establishing SS as the lower bound for transport.

those for fixed SS distance $= 0.1D_{\mathrm{m}}$ (black lines). Due to the high computational costs associated with a low viscosity-constrained timestep (Fourier condition), for $Re < 10$, we estimated the location of the transport threshold. This was done by simulating only a short initial transient. The non-transport threshold was then set when we observed a marked increase in the s_{x}–T slope. Thus, the use of CS or CC quantitatively shifts the phase boundaries, but retain their overall qualitative character.

Finally, SS distance is also a practically relevant measure in microfluidic transport settings where one is frequently concerned about proximity of objects to surfaces (be it particles, walls or other interfaces) and clearances. Indeed, this measure is robust to changes in geometry, such as changes in the shape of either master or slave, making CC distance less practical. We also exploited SS distance's robustness while designing the shapes of section 4.4 in the main text.

3.2. *Validation against baseline for viscous flow*

Our baseline simulations, seen in figure 6(a), are in good agreement with Gazzola *et al.* (2012). Our simulations slightly overpredict transport only at the transitional Re, an unsurprising observation given the sensitivity of the flow to physical and simulation parameters. We also include the inviscid characteristics in this plot to assay pure potential effects, and notice that viscous effects enhance baseline transport.

3.3. *Transitional Re*

We then gauge the sensitivity of the system response (trapping/non-trapping) to Re. We perturb the initial conditions by the same amount ($\pm 2\%$) as in the main text and draw the envelopes of the perturbed system characteristics for different Re. This is depicted in figure 6(b). We observe that cases within the transitional regime of ($78 \lesssim Re \lesssim 86$) are especially sensitive. The transitional case of $Re = 82$ is found to be the most sensitive. Beyond this transitional regime, the baseline becomes less sensitive to Re and initial positional perturbations.

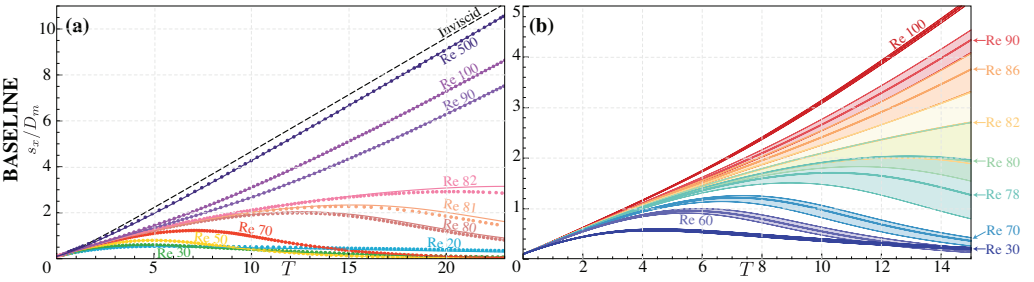

FIGURE 6. Baseline transport: Comparing the *(a)* separation distance s_x/D_m versus non-dimensional time $T = 2U_l t/D_m$ from our simulations (solid lines) to those of Gazzola *et al.* (2012) (dotted lines) indicates good agreement. *(b)* Sensitivity in the transitional regime ($78 \lesssim Re \lesssim 86$) to perturbations in the initial slave positions. We notice that the peak sensitivity occurs at $Re \sim 82$, which is the transition Reynolds number. We also depict system characteristics and sensitivity regions at representative $Re = 30, 60, 70, 90, 100$ for reference.

3.4. *Effect of inertia on both transitional boundaries (lower and higher Re limits)*

We address the effect of slave inertia, and provide a physical intuition to the observed contraction of the trapping region as D_s/D_m increases (figure 4 in the main text). At the Re considered in this paper, both pressure and viscous shear forces are important and are responsible for the slave's fluid-mediated motion. These forces act on the surface of the slave. The cumulative propulsive forces (obtained by integrating pressure and shear components along the slave's surface) then approximately scale linearly with the slave diameter D_s (since the cylinder circumference is πD_s). The inertia of the slave (proportional to its mass), however, scales with its area i.e. quadratically as D_s^2. Hence, the forces necessary to win inertia grow faster than the forces exerted by the fluid on the slave surface. Therefore, the trapping/no-trapping thresholds move inwards and narrow the trapping region, as inertia increases.

This minimal scaling relies on the assumption that the slave does not disrupt the flow generated by the master. This assumption was empirically verified during the course of the present work. An instance of such a verification can be found in section 4.4 of the main text where we design geometries with enhanced transport properties. Indeed, the bullet geometry was designed for transport enhancement without accounting for the finite-sized slave (i.e. we designed it by simulating the unperturbed streaming field). Yet upon testing it with a slave, we see a corresponding and expected improvement in transport. This observation indicates that the presence of the slave does not substantially modify the flow. Thus, our minimal scaling argument provides an intuition for the narrowing of the trapping region with increase in slave inertia, as observed in figure 4 of main text.

3.5. *Presence of lower and higher Re boundary*

We then look into the reasons behind the existence of the lower and higher Re transitional boundaries. The presence of the lower Re threshold is not straightforwardly intuitive. To explain this threshold, we observe the flow generated by a translating master and measure the pressure and viscous shear forces in the translation direction, at different Re across the trapping/non-trapping boundary. The goal is to track their individual contributions, report their behavior and relate them to the observed transport thresholds. For simplicity, and because of the arguments in section 3.4, we ignore the slave's presence. By the divergence theorem, the forces $\boldsymbol{F}$ acting on a parcel of fluid (of volume Ω and

boundary $\delta\Omega$) are

$$\boldsymbol{F} = \int_{\delta\Omega} \mathbf{T} \cdot \boldsymbol{n} dS = \int_{\Omega} \nabla \cdot \mathbf{T} dV \tag{3.1}$$

where $\boldsymbol{n}$ is the normal unit vector and $\mathbf{T}$ is the Cauchy stress tensor. For the incompressible, Newtonian fluid considered in this work,

$$\mathbf{T}(\boldsymbol{u}, p) = -p\mathbf{I} + \mu\left(\nabla \boldsymbol{u} + \nabla \boldsymbol{u}^T\right) \tag{3.2}$$

where p is the pressure, $\mathbf{I}$ is the identity matrix, μ is the dynamic viscosity and $\boldsymbol{u}$ is the fluid velocity.

Thus, the forces in the direction represented by the i^{th} tensor index read

$$\begin{aligned} F_i &= \partial_j T_{ji} \\ &= -\partial_j p \delta_{ji} + \mu \partial_j \left(\partial_j u_i + \partial_i u_j\right) \\ &= \underbrace{-\partial_i p}_{\text{Pressure forces}} + \underbrace{\mu \partial_j \partial_j u_i}_{\text{Viscous forces}} \end{aligned} \tag{3.3}$$

where the total force per unit volume F, is comprised of the pressure gradient and viscous shear forces. We report in figure 7 these forces at $T = 3$ (early transient) for a fluid parcel located where the slave would have been as predicted by our earlier transport simulations. In figure 7, the force field contours (pressure, viscous, and total) are shown for $Re = 10$, 30, 50 and 100 (spanning the trapping interval $17 \leqslant Re \leqslant 82$ for slaves with $D_\mathrm{s}/D_\mathrm{m} = 0.25$). We retain the same color range across these contours and note that orange corresponds to attractive forces and blue correspond to repulsive ones. Also marked by dashed lines is the predicted slave location, at which we measure all forces.

As can be seen, at the slave location and across the *Re* investigated, pressure forces are attractive. The role of pressure in attracting the slave is rather intuitive: as the master moves, it generates in the back a low-pressure region (this is well known for flow past cylinders or spheres). This low-pressure region generates a favorable pressure gradient that helps attract the slave, when placed in this flow field. On the contrary, viscous forces are repulsive and their effect monotonically decreases as the *Re* increases (since viscosity decreases).

These quantitative measurements are shown in the bottom plot of figure 7, as a function of *Re*. Red indicates pressure forces, blue indicates viscous forces and the total force is colored black. We see that pressure at the slave location achieves a maximum at $Re \sim 50$. As a result, the competition between pressure and viscous effects still presents a maximum in the total force, and decays to almost zero at low (10) and high (100) *Re* values. The presence of an attractive force maximum, and its consequent decay is the reason why we observe the trapping thresholds at low and high Reynolds numbers. Indeed, total forces need to win slave's inertia, once this is introduced in the flow. Moreover, combined with the scaling argument presented in section 3.4, the presence of this maximum also explains why the trapping boundaries move inwards (i.e. towards the maximum) as $D_\mathrm{s}/D_\mathrm{m}$ increases.

As an additional remark, in Gazzola *et al.* (2012) and in the present paper, we identified viscous effects as critical to enable transport, by performing corresponding computation in the potential flow regime and observing that transport was not enabled. This may at first seem in contradiction with the measurements reported in figure 7, in which pressure is attractive while viscous forces are repulsive. Nonetheless, there is no contradiction: indeed, viscous effects and associated no-slip condition on the master's surface are responsible for the formation of the wake, which in turn generates the low-

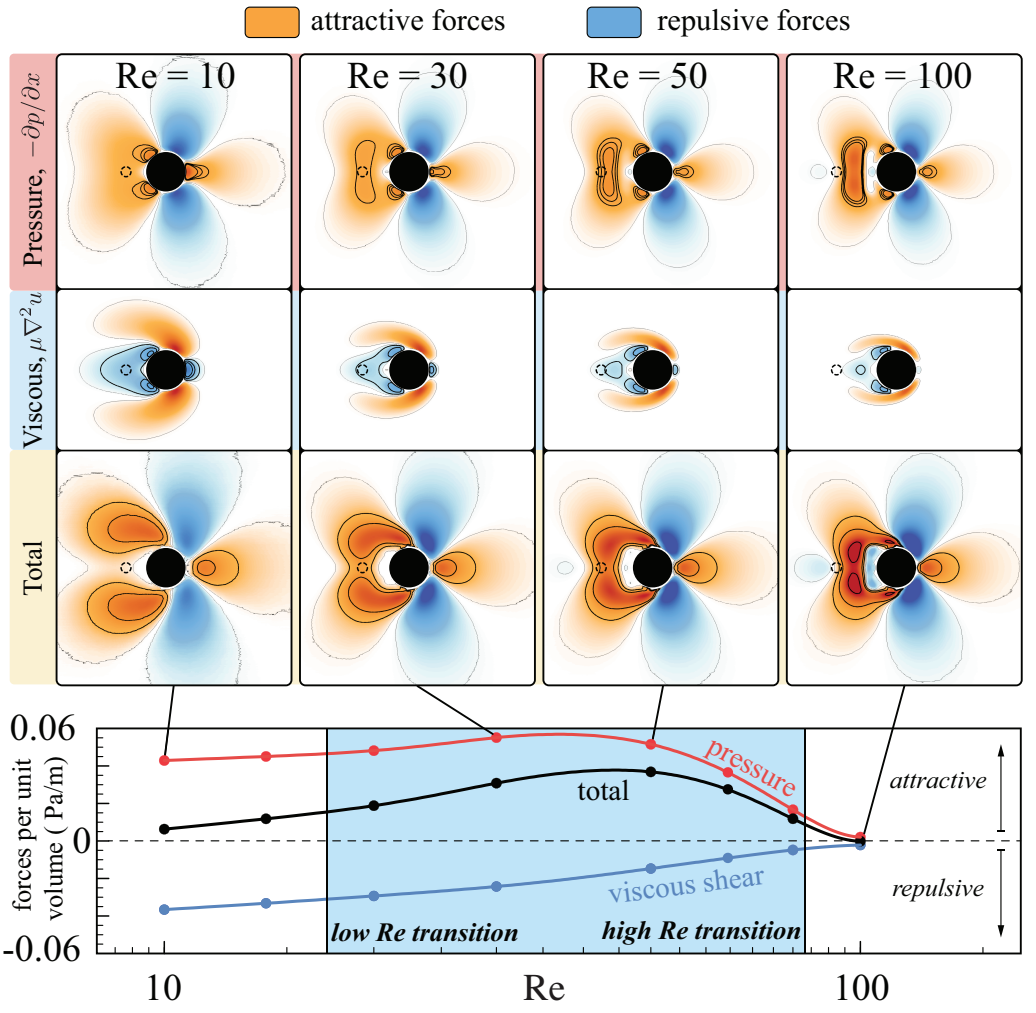

FIGURE 7. *(Top)* Contour plots comparing pressure, viscous and total forces for different *Re*, where orange represents attractive forces towards the master and blue represents repulsive forces away from the master. *(Bottom)* Plot comparing pressure (red), viscous shear (blue) and total (black) forces per unit volume, measured at the location where the slave would have been as predicted by earlier transport simulations, across different *Re*.

pressure region responsible for attracting the slave. Such a wake is not present in inviscid flows, hence their observed inability to "draw in" the slave for transport.

4. Enhancing transport with streaming

4.1. *Estimating the magnitude of streaming-generated forces*

We estimate that streaming generated forces for typical parameters are small, but not negligible—varying between $0.1 - 10\%$ of the wake-induced forces. An estimate of relevant forces per unit length induced by fluid flow past a static cylinder is given by $F = \frac{1}{2}C_{\mathrm{D}}(Re)\rho u^2$, the coefficient C_{D} being a function of only Re (Panton 2006). Thus the force contribution from the wake is roughly $F^{\mathrm{w}} = \frac{1}{2}C_{\mathrm{D}}(Re)\rho U_{\mathrm{l}}^2$ while streaming forces contribute forces on the order of $F^{\mathrm{s}} = \frac{1}{2}C_{\mathrm{D}}(R_{\mathrm{s}})\rho U_{\mathrm{s}}^2$ (the implicit assumption of

streaming flow being similar to a free-stream flow is justified as their time-scales are comparable). By definition, we have $U_\mathrm{s} = 2\epsilon\zeta U_\mathrm{l}$ and thus $R_\mathrm{s} = \epsilon\zeta Re$. Then, the ratio of these forces, couched in terms of ζ and Re for a fixed $\epsilon = 0.1$ is

$$\frac{F^\mathrm{s}}{F^\mathrm{w}} \sim \frac{0.04\zeta^2 C_\mathrm{D}(0.2\zeta Re)}{C_\mathrm{D}(Re)} \tag{4.1}$$

We now consider only $Re = 100$ for the purpose of exposition. With $\zeta = 0.25$ and with $C_\mathrm{D}(100) \approx 1.1, C_\mathrm{D}(5) \approx 3$ (Panton 2006), the ratio of forces is $\sim 0.2\%$. Considering a higher streaming intensity characterized by $\zeta = 2$, we have $C_\mathrm{D}(40) \approx 1.2$ (Panton 2006), leading to a force ratio of $\sim 17.4\%$. The order of the streaming forces are thus estimated to be in the range of 0.1–10%, justifying their non-negligible contribution in the evolution of the system dynamics.

4.2. *Characterizing transport in the presence of oscillations*

In the setting of streaming-enhanced transport, a typical $s_\mathrm{x} - T$ curve has oscillations, which reflect the oscillatory motion of the master. A naive calculation of ds_x/dT based on the instantaneous slope of such an $s_\mathrm{x} - T$ curve at some final time T_f, can mispredict transport. This is important, for example, in phase spaces exploring the effects of inertia (main text, §4.1), and while testing the robustness of streaming-enhanced transport (main text, §4.3). To account for these oscillations then, we measure ds_x/dT as an average, over the final two oscillation cycles:

$$\overline{\frac{ds_\mathrm{x}}{dT}} = \frac{\int_{T_i}^{T_f} \frac{ds_\mathrm{x}}{dT}(T)\, dT}{(T_f - T_i)} \tag{4.2}$$

where $T_f - T_i$ spans the time taken for two oscillation cycles.

However, for slaves not seeded on the symmetry axis (i.e. $\theta \neq \pi$), their two-dimensional trajectory renders the condition $\overline{ds_\mathrm{x}/dT} \leqslant 0$ prone to small numerical variations, for which slaves that are clearly transported are classified as left behind. One such example is shown in figure 8 for $Re = 82$, $\zeta = 0.5$ and $\theta = 1.1\pi$.

In the example of figure 8, the slave initially seeded off the symmetry axis approaches the master closely, long before the final time ($T_f = 28$) and then trails with the master for ~ 13 cycles. This slave is not considered as transported since $\overline{ds_\mathrm{x}/dT} = 7 \times 10^{-3} > 0$. Nevertheless, for all practical purposes, this slave is carried along. And even if $\overline{ds_\mathrm{x}/dT} = 7 \times 10^{-3}$ was not a numerical artifact due to oscillations, the slave would be transported till $T = 85$ (considering $s_\mathrm{x} = 0.5D_\mathrm{m}$ as a hard cutoff), equivalent in a typical microfluidic setting to 21 cm! In light of this, we then extend the transport condition to

$$\begin{gathered} \overline{\frac{ds}{dT}} \leqslant 0 \quad \text{(accelerating towards master)} \\ \textbf{or} \\ s < 0.1D_\mathrm{m} \ \text{ for any } T > 18 \quad \text{(close to the master in the last 10T)} \end{gathered} \tag{4.3}$$

In the above condition, we consider surface–surface distance s rather than s_x (i.e. projected onto the x-axis) to account for the two-dimensional nature of slave trajectories in cases with slaves initialized off the symmetry-axis. The second term of the above condition informs us that the slave trails closer than its initial distance for any time beyond the initial transient (i.e. last 10T). We could have introduced a tolerance here such as $\overline{ds/dT} \leqslant \epsilon$, but it is more arbitrary in our opinion. Instead, we simply check if the slave in the end is closer to the master than when it started. Hence to summarize,

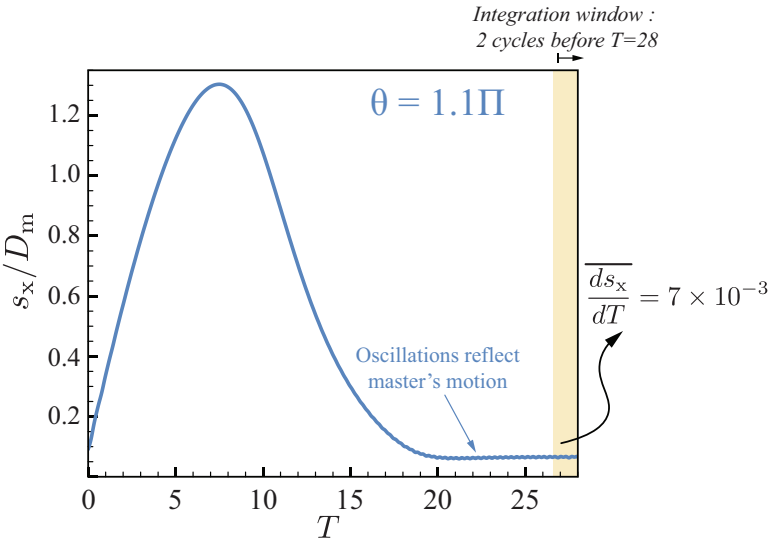

FIGURE 8. Insufficiency of $\overline{ds_x/dT} \leqslant 0$ as the sole transport condition for slaves initially placed off symmetry-axis. For the above example with $\theta = 1.1\pi$ at $Re = 82, \zeta = 0.5$, the slave is clearly transported yet $\overline{ds_x/dT} > 0$, due to master's unsteady oscillations.

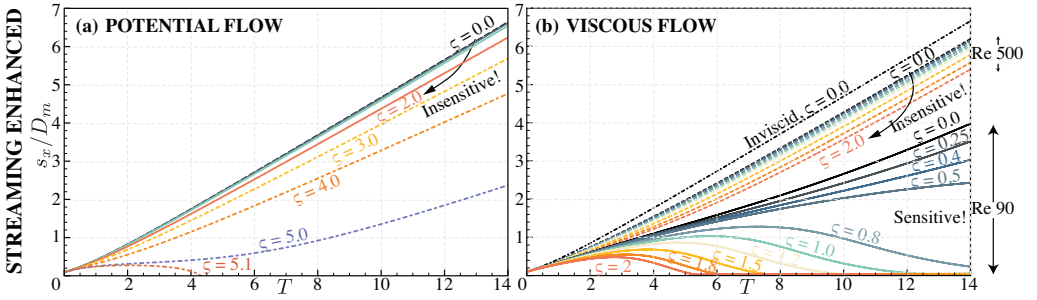

FIGURE 9. Streaming enhanced transport: (a) Enhancement in transport from pure potential effects is minimal and high ($\zeta \to 5$) values are required for trapping, while enhancement in the (b) viscous case is significant for finite Re, even at low ζ.

a slave initialized off the symmetry-axis is considered transported if it is accelerating towards the master, or it is already trailing close to it.

4.3. *Inviscid calculations: effect of oscillations and transitions*

We first investigate the transport characteristics arising from pure potential effects of the translation–oscillation strategy. We show these characteristics in figure 9a, for various ζ values. The system is initially insensitive to oscillations (and thus to perturbations in initial positions), while at high (> 5) ζ we are able to trap and transport the slave due to potential effects alone. This shows that while the primary transport enhancement mechanism observed in our studies can not be attributed to inviscid interactions, these effects are non-negligible at higher ζ values.

4.4. *Viscous calculations: effect of oscillations and transitions*

A key result of Gazzola *et al.* (2012) was that enabling viscous effects assist transport in the case of a linearly translating master cylinder (our baseline). In addition to this

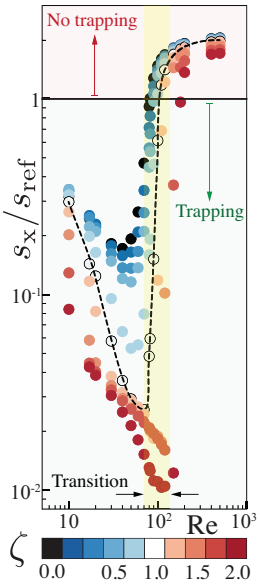

FIGURE 10. The plot of s_x/s_{ref} at $T = 10$ for a number of $(Re-\zeta)$ configurations illustrates how transport–enhancement translates across a wider range of Re. The dashed, black line connects configurations with $\zeta = 1$ and shows the transition from trapping to no-trapping behavior. The steepness of this line around $Re \approx 100$ illustrates that the system still retains its sensitivity to Re variations. This behavior is seen across all ζ, and the corresponding sharp transition region (across all cases) is highlighted.

result, we find that the effect of oscillations in enhancing the ability of slave transport is amplified in a viscous regime. This is clearly seen when comparing figure 9a and figure 9b for some oscillation intensity (fixed ζ). As seen in the main text, this enhancement can be attributed predominantly to the viscous streaming response. Using streaming, we perturb the slave's dynamics enough to fall in the transitional regime of figure 6(b) at which point the first order linear motion of the master can trap the slave. This is highlighted in figure 9b for the case of $Re = 90$ at various ζ values. We also call attention to the insensitivity in the characteristics at a high Re of 500, an unsurprising observation as we move towards the inviscid approximation. We further undertake a parametric investigation to characterize the effect of superimposing oscillations, systematically spanning Re between 10–500 and ζ between 0–2. We depict this in figure 10, where we plot s_x/s_{ref} (at $T = 10$) against Re, for different ζ. Here s_{ref} is the separation distance (at the same time $T = 10$) of the reference baseline at $Re \approx 82$, i.e. at the transition between transport and non-transport simulations when oscillations are not active (i.e. $\zeta = 0$). This qualitatively means that cases in figure 10 with $s_x/s_{ref} < 1$ transport the slave. We then observe that while oscillations always assist transport, higher ζ values are necessary for trapping at higher Re, and beyond $Re \approx 200$ oscillations are no longer able to drive the system into the transport regime, and the slave is then left behind. The system still retains its inherent sensitivity to Re, apparent from the sharp jump between trapping/non-trapping cases across $100 \lessapprox Re \lessapprox 200$, for any fixed ζ. We highlight this for the configurations with $\zeta = 1$, all connected together by a black dashed line in figure 10. We observe that a small change in Re (around the transitional Re, from $100 - 110$ in this particular case) changes the system behavior from trapping to non-trapping. This is reflected in figure 10 by the steepness of the dashed line mentioned above, around the transitional Re. We

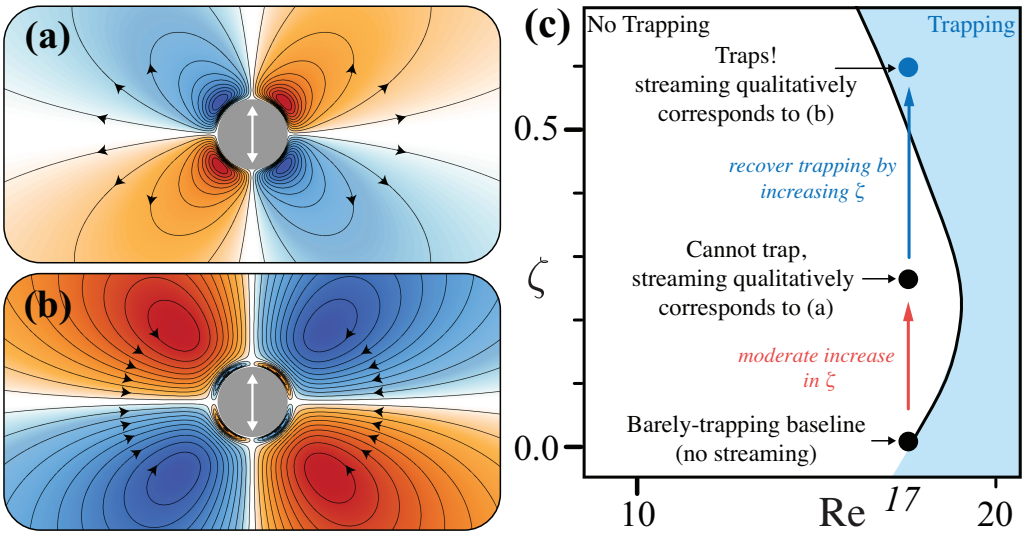

FIGURE 11. The pure streaming flow fields visualized for *(a)* low R_o (lower ζ) and *(b)* high R_o (higher ζ), illustrating the change of flow velocity directions (black arrows) as ζ is increased. This translates to initial adverse effect on transport observed in the phase space of *(c)* for a moderate increase in ζ, where streaming qualitatively corresponds to *(a)*. Upon further increasing ζ, streaming elicits the favorable flow field of (b), thus enabling trapping as seen in (c).

note this behavior is preserved across all ζ, depicted as the transition region in figure 10.

4.5. *Existence of adverse effect on transport*

As observed in figure 4 of the main text, a phase with adverse effect on transport exists at low limits of *Re*. Moreover, the trapping/non-trapping threshold at lower *Re* first shows a negative effect with increasing ζ, and then a positive effect (figure 11(c)). Here we relate the existence of the adverse phase as well as the above negative effect to streaming flows. We draw attention to the fact that both these behaviors are observed at low *Re* and low ζ limits, and thus at low oscillatory Reynolds numbers R_o (where $R_o = \zeta \cdot Re$). At such low values of R_o, the streaming field presents only one boundary layer stretching to infinity (figure 11(a)), as opposed to the double boundary layer structure characteristic of higher R_o (hence higher ζ, seen in figure 11(b)). Because of this, in the lower R_o regime, the streamlines due to viscous streaming are directed away from the master (figure 11(a)), hence they are not favorably oriented for transport. This particular flow pattern characteristic of low R_o is well-known, and we accurately reproduce this in our simulations as illustrated in the comparison with experiments (Lieu *et al.* 2012) and analytical (Bertelsen *et al.* 1973) results of figure 2 in the main text.

Here, we make use of figure 11, to further clarify this in relation to the ζ–*Re* phase space presented in figure 4 of the main text. Figure 11(b) corresponds to the streamlines of a representative case with a moderate R_o of $O(5)$–$O(100)$, which we constructively utilized for transport, thanks to the favorable streaming field direction (streaming draws the slave in, towards the master, as indicated by the arrows). Figure 11(a) instead corresponds to lower values of R_o, from $O(1)$–$O(5)$, wherein the characteristic streaming field is directed such that it pushes the slaves away from the master (once again, the arrows indicate the velocity direction).

It is then not surprising that, when we add this repelling streaming component to any

Re	Baseline	Streaming-enhanced
17	20%	38%
50	59%	59%
82	69%	78%
90	61%	82%

TABLE 1. Percentages of slaves transported across Re, for condition $\overline{ds/dT} \leqslant 0$ (or) $s < 0.1D_{\mathrm{m}}$.

barely-trapping transitional baseline(s) at the lower Re limit (for any $D_{\mathrm{s}}/D_{\mathrm{m}}$ ratio), an adverse effect on transport is observed. This is shown in figure 11(c), for $D_{\mathrm{s}}/D_{\mathrm{m}} = 0.25$, where for a moderate ζ applied to the transitional baseline $Re = 17$, trapping is not achieved. To recover trapping then, we need to increase ζ (hence increase R_{o}) further, so as to elicit the favorable streaming response of figure 11(b). This is also marked in our phase space (figure 11(c)).

We note that the existence of the adverse phase and the observed negative effect is in line and consistent with the fact that streaming-induced streamline contraction is the basis of transport enhancement. Indeed, in the adverse cases we do not have this contraction, but the opposite—streamlines are more spaced apart (figure 11(a) vs figure 11(b)).

Finally, we add that both these phenomena are not observed at high Re. In fact, in this limit, streaming is always favorably directed for transport. This is consistent with the phase space of figure 4 (main text) and provides yet another hint that streaming-induced streamline contraction is the responsible transport mechanism.

4.6. *Transport enhancement in azimuthally seeded slaves*

We further test the reliability of streaming for transport enhancement by initializing the slaves at different azimuthal positions and compare the transport efficiencies (defined as the ratio of transported to total initialized slaves) and the rate of transport for $\zeta = 0$ and $\zeta = 0.5$ across different Re.

Using the mathematical condition for transport defined in section 4.2, we measure and identify slaves that are transported (trajectories marked in blue) and not transported (trajectories marked in red) as shown in figure 12. The final time chosen ($T_f = 28$) is sufficiently long to determine whether the slave is transported or not, as we observe steady, consistent transport behavior (according to the definition above) across all slaves for $14 \leqslant T \leqslant 28$. We then compare the transport efficiencies for different Re and observe that streaming consistently performs comparably or better than baseline cases. The percentage of slaves trapped with this criterion is reported in table 1 and on the top right of each trajectory plot in figure 12. As can be seen, the only case in which we do not observe an improvement (but also no degradation) is at $Re = 50$ for which the baseline case is already effective at transport.

We also highlight that the initial azimuthal position is important in the context of streaming-enhanced transport. In the cases with streaming, all the slaves within a 110^o cone behind the master (marked in blue in figure 12) are transported, across all Re. This is not true in the baseline cases. Indeed, when streaming is compared to the baseline across different Re, transport efficiency is always either preserved or enhanced (up to 69% at Re=90, see table 2). From a practical perspective, this means that if one can place a particle approximately behind the master, streaming is very effective in enabling transport. This is useful in microfluidic applications where slaves can be easily seeded in

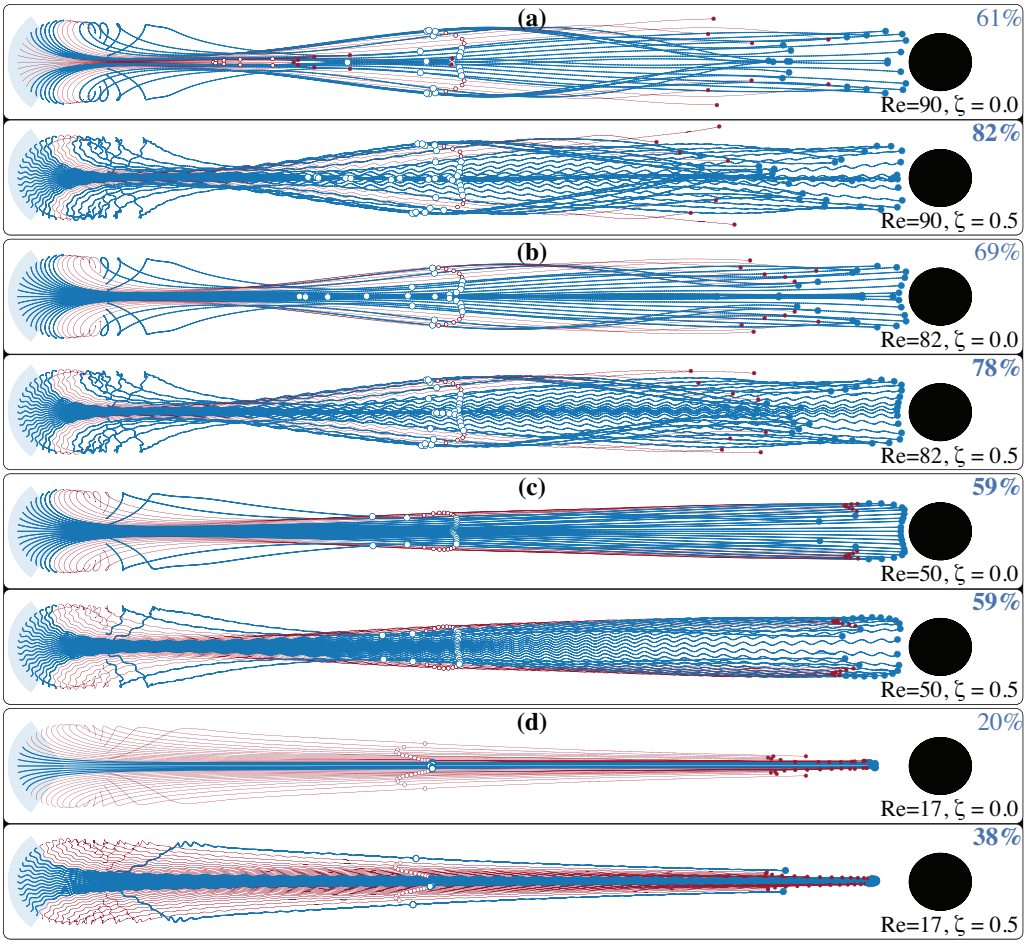

FIGURE 12. Robustness of the streaming strategy across different Re in transporting slave initialized around the master. Blue trajectories indicate slaves that are successfully transported while red indicate slaves that are not transported. The positions of the slaves at $T = 14$ and $T = 28$ are marked using hollow and filled circles respectively. The percentge on the top right of each panel indicates the transport efficiencies of the master computed at $T = 28$. We note that in the streaming enabled cases, all slaves within a 110^o cone (marked with a transparent blue cone in each of the cases) behind the master are transported, while this is not so for cases without streaming.

the back of the cylinder, but due to experimental uncertainties, not necessarily on the symmetry axis.

Next, we look at the rate at which slaves are attracted to the master as another transport metric. Streaming generally enhances this rate (the only exception is the case which lies in the adverse region discussed in section 4.5). While this was shown for cases initially aligned with the symmetry axis in the main text (figure 3(d)–(g)), it is not apparent for cases shown in figure 12. We then depict this in figure 13 for cases with slaves initially not aligned with the symmetry axis and within the 110^o cone of trapping. In this figure, we show the transport characteristics for three cases with different initial azimuthal locations (θ, specified in the inset) for cases with and without streaming. As can be seen, streaming quickens transport for slaves placed at various initial locations within the cone region, as the oscillation intensity ζ increases.

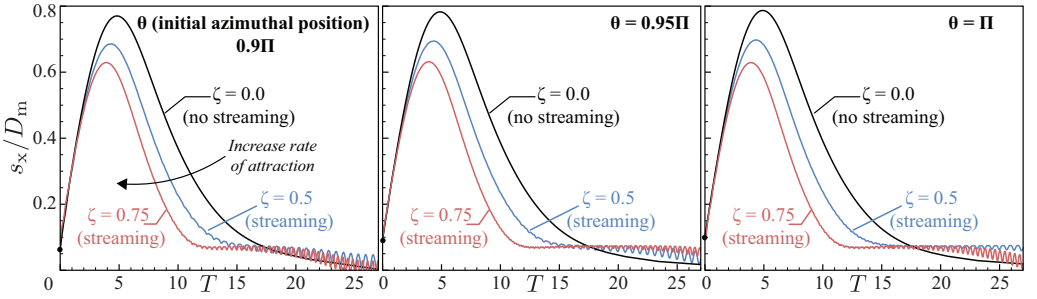

FIGURE 13. Transport characteristics for no-streaming (black lines) and streaming-enabled cases (blue lines with $\zeta = 0.5$; red lines with $\zeta = 0.75$) for slaves initially placed off the symmetry axis as indicated by θ in the inset.

Re	Baseline	Streaming-enhanced
17	61%	100%
50	100%	100%
82	100%	100%
90	31%	100%

TABLE 2. Percentage of trapped slaves initialized within the blue cone, for condition $\overline{ds/dT} \leqslant 0$ alone. Streaming always either preserves or increases efficiency.

In conclusion, the above demonstrations indicate that: (a) streaming enables and enhances transport across *Re* in practically relevant cases, and (b) it increases the rate at which slaves are drawn closer to the master.

4.7. *Robustness to radial perturbations*

Streaming has been shown to be a robust strategy with respect to the initial azimuthal positions of the slave. Here we consider the same setup, restricting the investigation to $Re = 90, \zeta = 0.5$ while adding a $\pm 2\%$ (radial) perturbation in the initial surface–surface distance between the master and the slave. The results are shown in figure 14. Streaming-based transport is also robust to radial perturbations. The only significant difference is seen in the trajectories of cases with $|\pi - \theta| \lesssim \pi/5$, due to the transitional nature of the baseline as stated in the main text.

4.8. *Design: spline parametrization*

We construct the bullet profile (presented in the main text) of semi-major dimension r by using a spline-based shape parametrization, similar to Rossinelli *et al.* (2011). The piecewise-cubic spline (figure 15) is fit in the polar coordinates (with restricted domain on $\theta \in [0, \pi]$), after choosing n control points and specifying their radial k_i and angular α_i positions. We enforce periodicity and top–bottom symmetry by specifying zero-slope (clamped) boundary conditions for the half-spline and mirroring it about its central axis. Our freedom in the choice of n and consequently the set of $\{k_\mathrm{i}, \alpha_\mathrm{i}\}$ (with cardinality/degrees of freedom $= 2n$) renders it possible to get shapes with desired (high) curvatures.

We tabulate the parameters used for constructing the bullet and other profiles used in the manuscript in table 3. We note that across all splines, k_1 and k_n (the scaling lengths of the diametrically opposite points) are identically set to 1.0 to ensure invariance in the

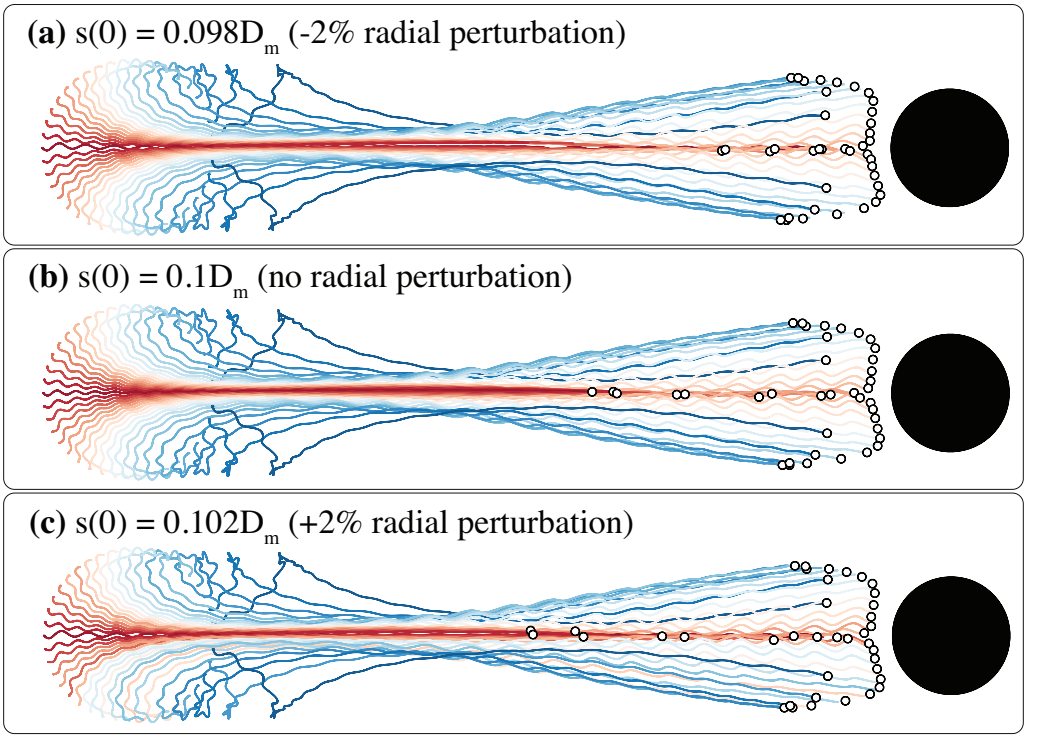

FIGURE 14. Robustness of the streaming strategy to perturbations of the initial radial positions of seeded slaves

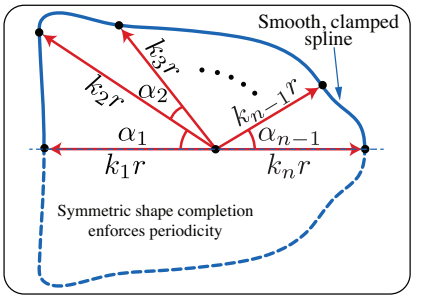

FIGURE 15. Construction of the smooth,periodic piece-wise cubic spline with given inputs $\{k_i, \alpha_i\}$

major dimensions of the shape. We then use this invariant dimension to define our *Re* and quantities derived from it.

4.9. *Transport enhancement in three dimensional viscous flow*

We conduct a baseline study on the performance of the spherical master across different *Re* and observe better transport as *Re* decreases (figure 16a), but no trapping is achieved. We proceed to examine the usefulness of streaming effects by introducing oscillations ($\zeta = 0.5, 1.0, 2.0$) for the representative case of $Re = 20$. While figure 16b suggests slight improvement in transport with increasing ζ, it is evident that no trapping occurs. Looking into the streamlines of the cases without ($\zeta = 0$) and with ($\zeta = 2.0$) oscillations, we see there is barely any streamline contraction in the oscillation plane (figure 16c) and while

Spline ref.	n	$\{k_i\}$	$\{\alpha_i\}$ (in ^{o})
Bullet	7	$\{1.00, 1.40, 1.42, 1.39, 0.72, 0.95, 1.00\}$	$\{43.0, 1.0, 1.0, 35.0, 90.0, 10.0\}$
figure 7b (in main text)	6	$\{1.00, 1.28, 1.31, 1.29, 1.00, 1.00\}$	$\{41.5, 1.75, 1.75, 60.0, 75.0\}$
figure 7c (in main text)	6	$\{1.00, 1.40, 1.42, 1.40, 0.99, 1.00\}$	$\{43.0, 1.0, 1.0, 45.0, 90.0\}$

TABLE 3. Parameters for the splines used in the manuscript

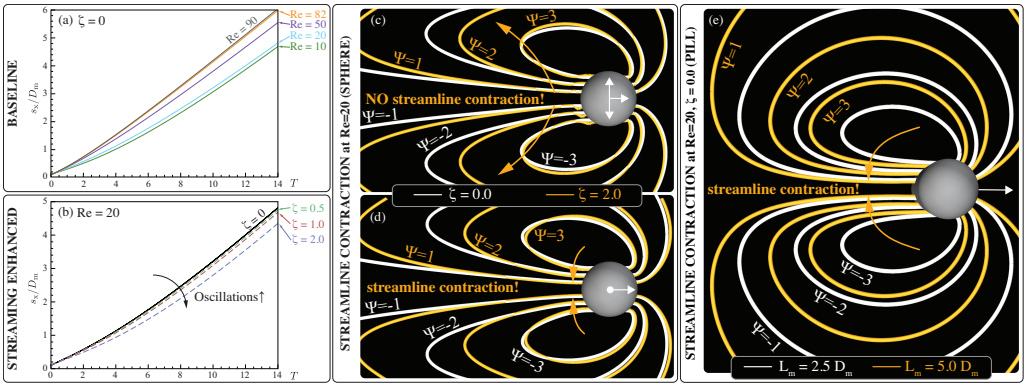

FIGURE 16. Separation distance s/D_m versus non-dimensional time $T = 2U_l t/D_m$ for (a) baseline transport at different Re and (b) streaming-enhanced transport with different ζ at $Re = 20$. Comparing the streamlines for the case using spherical master without ($\zeta = 0$, white streamlines) and with ($\zeta = 2$, orange streamlines) oscillation at Re = 20 reveals that streamline contraction does not happen on the (c) oscillation plane and barely occur on the (d) plane perpendicular to the oscillation plane (ψ values scaled-up by 1250). Comparing the cases using linearly-translating pill-shaped master of different lengths L_m without oscillation reveals streamline contraction.

slightly more streamline contraction occurs on the plane perpendicular to the plane of oscillation (figure 16d), the acceleration in the wake flow provided is not sufficient to achieve transport.

We elongate the master sphere to form a pill-shaped master of D_m with hemispherical caps having an end-to-end length L_m. At $Re = 20$, pill set in linear motion shows improvement in transport as L_m increases. We notice that mere increment in L_m promotes streamline contraction in systems of linearly-translating pill (figure 16e), and we can further enhance it by introducing oscillations.

REFERENCES

ATKINSON, KENDALL E 1967 The numerical solution of fredholm integral equations of the second kind. *SIAM Journal on Numerical Analysis* **4** (3), 337–348.

BERTELSEN, A, SVARDAL, ASLAK & TJØTTA, SIGVE 1973 Nonlinear streaming effects associated with oscillating cylinders. *Journal of Fluid Mechanics* **59** (03), 493–511.

GAZZOLA, M., CHATELAIN, P., VAN REES, W.M. & KOUMOUTSAKOS, P. 2011 Simulations of single and multiple swimmers with non-divergence free deforming geometries. *Journal of Computational Physics* **230** (19), 7093–7114.

GAZZOLA, MATTIA, MIMEAU, CHLOE, TCHIEU, ANDREW A & KOUMOUTSAKOS, PETROS 2012 Flow mediated interactions between two cylinders at finite re numbers. *Physics of Fluids* **24** (4), 043103.

KOTAS, C.W., YODA, M. & ROGERS, P.H. 2007 Visualization of steady streaming near oscillating spheroids. *Experiments in fluids* **42** (1), 111–121.

Lamb, Horace 1932 *Hydrodynamics*. Cambridge university press.

Lieu, Valerie H, House, Tyler A & Schwartz, Daniel T 2012 Hydrodynamic tweezers: Impact of design geometry on flow and microparticle trapping. *Analytical chemistry* **84** (4), 1963–1968.

Lutz, Barry R, Chen, Jian & Schwartz, Daniel T 2005 Microscopic steady streaming eddies created around short cylinders in a channel: Flow visualization and stokes layer scaling. *Physics of Fluids (1994-present)* **17** (2), 023601.

Munnier, Alexandre & Pinçon, Bruno 2010 Locomotion of articulated bodies in an ideal fluid: 2d model with buoyancy, circulation and collisions. *Mathematical Models and Methods in Applied Sciences* **20** (10), 1899–1940.

Nair, Sujit & Kanso, Eva 2007 Hydrodynamically coupled rigid bodies. *Journal of Fluid Mechanics* **592**, 393–411.

Panton, Ronald L 2006 *Incompressible flow*. John Wiley & Sons.

Rossinelli, D., Chatagny, L. & Koumoutsakos, Petros 2011 Evolutionary optimization of scalar transport in cylinder arrays on multigpu/multicore architectures. *Evolutionary and Deterministic Methods for Design, Optimization and Control* pp. 773–784.

Sbalzarini, Ivo F, Walther, Jens H, Bergdorf, Michael, Hieber, Simone Elke, Kotsalis, Evangelos M & Koumoutsakos, Petros 2006 Ppm–a highly efficient parallel particle–mesh library for the simulation of continuum systems. *Journal of Computational Physics* **215** (2), 566–588.

Tchieu, AA, Crowdy, D & Leonard, A 2010 Fluid-structure interaction of two bodies in an inviscid fluid. *Physics of Fluids* **22** (10), 107101.